Lithospheric contraction on Mars: A 3D model of the Amenthes thrust fault system

A. Herrero-Gil[1], J. Ruiz[1], I. Romeo[1]

[1] Departamento de Geodinámica, Estratigrafía y Paleontología. Universidad Complutense de Madrid, 28040 Madrid, Spain.

Corresponding author: Andrea Herrero-Gil (andreaherrero@ucm.es)

Key Points:

- A 3D forward model combining fault parallel flow and trishear gives listric fault geometries at depth for the Amenthes thrust fault system.
- Major faults root at 20–24 km deep, interpreted to be the brittle-ductile transition, while secondary faults root at 10.5–13 km.
- Considering secondary faults increases regional shortening by 60 to 200%, implying higher global contraction than previously estimated.

Abstract

Amenthes Rupes is the topographic expression of a main fault belonging to a thrust fault system located parallel to the martian dichotomy boundary. A 3D forward model has been applied to the Amenthes thrust fault system, constraining fault geometries at depth, variations of slip along strike and structural parameters controlling the formation of fault propagation folds. Our results provide a complex 3D view of the tectonic framework of the area, with implications for tectonic evolution, regional shortening distribution, and the main mechanical discontinuities in the lithosphere. The modeled fault surfaces show planar morphologies combined with listric geometries at depth. The obtained depths of faulting for the major faults of this fault system suggest a depth of the brittle-ductile transition (at the time of formation) of 20–24 km, somewhat shallower than previous estimates for this area. A possible mechanical discontinuity located at 10.5–13 km deep can be deduced from the faulting depths of the secondary faults. The listric geometries at depth imply that slip is transmitted from the decollement, together with the inclusion in the model of secondary and subsidiary faults, allow us to estimate the horizontal shortening recorded in this area ranging from 2-3 km up to ~5.5 km in the southeastern part of the fault system. This range increases the previous shortening estimates in this area between ~60 and ~200%. Consequently global shortening estimates based on global fault maps are biased by the detail of mapping, and shortening would substantially increase if secondary faults were included.

Plain Language Summary

Amenthes Rupes is a large topographic relief known as a lobate scarp, formed by the displacement of a contractional fault belonging to a fault system located in the Amenthes Region, Mars. The study of the faults forming these reliefs provides insights on the faulting and folding processes, which are related to the state of the lithosphere at the time of formation. A 3D modeling has been applied to Amenthes fault system, modeling fault geometries at depth, interaction between faults, associated slip values, depth of faulting, and other parameters that control the formation of the relief. These results provide a complex 3D view of how the area contracted. The obtained fault surfaces show curved geometries at depth. The major faults in the fault system root at a depth where ductile deformation in the lithosphere begins, estimated to be at 20–24 km. The estimated regional horizontal shortening accommodated by the fault system range between 2 and ~5.5 km, which increases the shortening in this area between 60 and 200% compared with previous estimates. This recognizes that the inclusion of secondary faults in global contraction models would increase substantially the global shortening estimates.

1 Introduction

Lobate scarps are positive structural reliefs observed on terrestrial planetary surfaces, assumed to be the expression of large thrust faults (e.g. Anguita et al., 2006; Schultz & Watters, 2001; Strom et al., 1975; Watters & Nimmo, 2010; Watters & Robinson, 1999). These structures present an asymmetric relief that shows the characteristic morphology of a fault related fold caused by the displacement of a low angle thrust fault breaking the topographic surface. The lobate scarp uplift is formed by an anticline with a gentle trailing flank (backlimb), and a frontal abrupt flank forming the scarp face (forelimb). A trailing syncline and a frontal syncline are usually present on each side of the anticline (e.g. Grott et al., 2007; Herrero-Gil et al., 2019, 2020; Schultz, 2000; Schultz & Watters, 2001). The large thrust faults underlying lobate scarps

have been studied and modeled by several authors on different terrestrial bodies like Mars (e.g. Egea-González et al., 2017; Grott et al. 2007; Herrero-Gil et al., 2019; 2020; Klimczak et al., 2018; Mueller et al., 2014; Ruiz et al., 2008; Ruj et al., 2018; Schultz & Watters, 2001), Mercury (e.g. Crane & Klimczak, 2019; Egea-González et al., 2012; Galluzzi et al., 2015, 2019; Giacomini et al., 2019; Semenzato et al., 2018; Watters et al., 2002), the Moon (e.g. Byrne et al., 2015; Williams et al., 2013), Ceres (Ruiz et al., 2019) and asteroid 433 Eros (Watters et al., 2011). These works usually include the study of the timing of faulting and the analysis of the structural parameters that define the fault morphology and kinematics (depth of faulting, dip angle, fault slip), with the final aim of advancing on the knowledge of the tectonic and thermal evolution of these terrestrial bodies. The modeling of the structural parameters is performed assuming that fault geometry and fault slip control lobate scarp topography (Schultz & Watters, 2001; Watters et al., 2002). The study of martian lobate scarps provides insights on the rheology of the martian lithosphere at the time of formation (Ruiz et al., 2008). The depth of faulting of the large underlying faults has been related to a main rheological discontinuity, that on Mars is considered to represent the brittle-ductile transition (BDT) at the time of lobate scarp formation (e.g., Grott et al., 2007; Ruiz et al., 2008, 2009, 2011; Schultz & Watters, 2001).

The most studied lobate scarp on Mars is Amenthes Rupes (e.g. Egea-González et al., 2017; Mueller et al., 2014; Ruiz et al., 2008; Schultz, 2003; Schultz & Watters, 2001; Watters et al., 2000), due to its large dimensions and its location near the dichotomy boundary (Watters, 2003b) (Fig. 1), which makes its study essential when analyzing the mechanical and thermal properties, and the evolution of the lithosphere (e.g. Egea-González et al., 2017; Ruiz et al., 2011; Schultz & Watters, 2001). The Amenthes Rupes lobate scarp, as well as most of the lobate scarps modeled on Mars, has been modeled through 2D cross sections analysis (e.g. Egea-González et al., 2017; Grott et al., 2007; Herrero-Gil et al., 2019; Mueller et al., 2014; Ruiz et al., 2008; Schultz & Watters, 2001). This 2D modeling applied to lobate scarps restricts the results obtained to the chosen cross sections of structures that are hundreds of kilometers long and present significant variations along their length (e.g. Herrero-Gil et al., 2020; Klimczak et al., 2018). Besides, Amenthes Rupes is not formed by an isolated fault. This is the largest structure belonging to a structural set of surface breaking thrust faults (Schultz, 2003; Watters & Robinson, 1999) located in the Amenthes Region (Fig. 1). The complexity of the interaction between these faults and the main Amenthes thrust fault controls the topographic expression of lobate scarps in this area.

The 3D modeling of lobate scarps allows expansion of our knowledge of the fault geometries at depth and fault kinematics, and of the mechanical structure of the lithosphere at the time of formation (Herrero-Gil et al., 2020). Here we show the results of a detailed 3D modeling of the Amenthes thrust fault system providing information about the fault geometries and fault related folding, together with the variations of the structural parameters along their strike and with depth and the interaction between faults, resulting in a complex tectonic framework. This 3D procedure provides a step forward in the understanding of thrust fault systems on Mars compared with previous 2D approaches. The depth of faulting of the main modeled faults provides estimates of the BDT depth at the time of formation. In addition, the study of the secondary and subsidiary faults provides information about the presence of mechanical discontinuities in the crust. This analysis also provides insights about the nature of the deformation in this region close to the martian dichotomy boundary, as well as about the general processes that formed martian lobate scarps and the amount of horizontal contraction implied (the terms “contraction” and “contractional structures” are used through the text in the sense of

structures generated by linear horizontal contractional deformation, i.e. shortening), which in turn has implications for the tectonic and thermal evolution of Mars.

1.1 Amenthes Rupes

Amenthes Rupes is located in the heavily cratered highlands of Mars (e.g. Caprarelli et al., 2007; Erkeling et al., 2011; Mueller et al., 2014; Schultz, 2003; Schultz & Watters, 2001; Watters, 2003b), specifically in the northeast of the Amenthes Region. This topographic structure is the morphological expression of the displacement on a large thrust fault with surface rupture (e.g. Mueller et al., 2014; Schultz & Watters, 2001). The main thrust fault that forms Amenthes Rupes is part of an array of five thrust faults underlying a set of lobate scarps (Schultz, 2003; Watters & Robinson, 1999), striking 120–140ºE (Fig. 1), parallel to the NE margin of Amenthes Planum (Caprarelli et al., 2007) which is located southwest.

The Amenthes Rupes lobate scarp was formed in the Late Noachian/Early Hesperian (e.g., Schultz & Watters, 2001; Watters & Robinson, 1999), around 3.7 Ga ago (Egea-González et al., 2017). The Late Noachian highland crust, where lobate scarps formed, is expected to be formed by non-layered rocks with more isotropic character than the Amazonian-Hesperian units that postdate them (e.g. Schultz, 2000; Mueller et al., 2014). Martian erosion rates have remained very low from Hesperian to the present (e.g. Golombek & Bridges, 2000; Golombek & Phillips, 2010) and this area does not show significant signs of erosion affecting the lobate scarps. However, the structural relief related to this fault system was modified by several impact craters, some of them clearly postdating its formation. A geological unit of Amazonian-Hesperian age postdates the Late Noachian cratered terrains, forming smooth plains in the areas of low topographic relief, as well as infilling most of the craters (Erkeling et al., 2011).

Amenthes Rupes has aroused great interest due to its proximity to the dichotomy boundary. This is the largest of a series of lobate scarps located between 100 and 500 km southwest of the dichotomy boundary, in the highlands of Arabia Terra, Amenthes Region and Terra Cimmeria. These lobate scarps are roughly parallel to the dichotomy boundary and record a contractional strain perpendicular to this boundary (e.g. McGill & Dimitriou, 1990; Nimmo, 2005; Watters, 2003a, 2003b; Watters & Robinson, 1999; Watters et al., 2007). The deformation along the dichotomy boundary in these areas occurred during the Late Noachian and Early Hesperian (McGill & Dimitriou, 1990; Nimmo, 2005; Ruiz et al., 2008: Watters and Robinson, 1999) postdating the formation of the dichotomy boundary but being important in the shaping of its current relief. These observations suggest that the formation of the lobate scarps in these areas is related to the dichotomy boundary (Watters & Robinson, 1999), which has been associated with lithospheric flexure (Watters, 2003a; Watters & McGovern, 2006). The formation of Amenthes Rupes has been also related to Isidis basin due to its radial orientation with respect to the basin center (Wichman & Schultz, 1989). Egea-González et al. (2017) included Amenthes Rupes in their circum-Hellas study since it presents a concentric orientation to Hellas basin, being orthogonal to a compressive stress associated with this large impact basin. Similar contractional structures parallel to Amenthes Rupes can be found closer to Hellas basin (Cerberus Dorsa). Previous studies focused on modeling Amenthes Rupes had as a main objective the calculation of the depth of faulting of the underlying fault, which on Mars is assumed to coincide with the BDT at the time of faulting. This BDT depth has been used to model the thermal structure of the early martian lithosphere and to calculate the heat flow values

during the Late Noachian/Early Hesperian (Egea-González et al., 2017; Mueller et al. 2014; Ruiz et al., 2008, 2011; Schultz & Watters, 2001).

The Forward Mechanical Dislocation method (FMD) (Toda et al., 1998, 2005) that models the surface as an elastic halfspace, and the Balanced Cross Sections method (BCS) (Chamberlin, 1910, 1919; Dahlstrom, 1969) based on mass conservation, are the two approaches previously applied to model 2D topographic profiles across Amenthes Rupes. Although non-planar fault morphologies (listric fault geometries) have been proposed to explain lobate scarp formation (Mueller et al., 2014; Watters & Nimmo, 2010), previous works that have modeled Amenthes Rupes with FMD method present the fault plane as a planar surface with a constant dip, because the results obtained using non-planar geometries did not provide satisfactory results (Schultz & Watters, 2001). Schultz and Watters (2001) modeled two cross sections of Amenthes Rupes with FMD method to obtain a depth of faulting of 25–30 km. The same method was later applied by Ruiz et al. (2008) to a perpendicular cross section obtaining a depth of faulting of 27–35 km, and by Egea-González et al. (2017) to obtain a depth of faulting of 27–33 km. The BCS method was used by Mueller et al. (2014) proposing a listric fault, due to the topographic characteristics of the lobate scarp, obtaining a depth of faulting of 33–48 km.

2 Data and method

The objective of the 3D modeling of lobate scarps is to obtain the fault geometries, the slip distribution and trishear parameters that best replicate the topographic surface uplifted by each fault with the smallest misfit with the observed topography. A detail mapping of the studied structures is necessary before the modeling process to identify the fault structures of the area. The topographic base used for the mapping and modeling of Amenthes thrust fault system is the Mars Orbiter Laser Altimeter data (MOLA, Mars Global Surveyor) with a ~463m/px (Smith et al., 2001; Zuber et al., 1992). The main base image used during mapping is the Thermal Emission Imaging System (THEMIS, Mars Odyssey mission) daytime infrared (IR) model with a 100 meter/pixel resolution (Christensen et al., 2004). The Context Camera images (CTX, Mars Reconnaissance Orbiter) (Malin et al., 2007) have been consulted occasionally. The analysis of the MOLA topography, together with THEMIS and CTX images, allowed us to make a detailed structural map of the area (Fig. 1). The identification of the tectonic structures in the area was performed by analyzing several profiles, attending to slope changes to identify the reliefs that may be related to tectonic deformation. THEMIS images (or CTX images when more resolution was needed) were used to verify their tectonic origin and to trace them in the map. The five large thrust faults underlying the reliefs that meet the description of lobate scarp, together with their associated fold structures, were mapped following this procedure. Other minor contractional structures have been identified in the area. The minor thrust faults have been distinguish from wrinkle ridges because it was possible to identify the vergence of the structure due to the uplift of the hanging wall. Nevertheless, wrinkle ridges present a lower relief and a complex structure that requires an exhaustive analysis to identify the vergence of the underlying thrust faults, which is not the objective of this work, so we have kept this morphological term in the structural map.

The folding associated with thrust fault generation has been considered, in this study, to be caused by fault propagation folding since the morphologies of other fault related folds, like fault-bend folds and detachment folds, do not match the observations (Jamison, 1987). Displacement-gradient folds (Wickham, 1995) have been proposed to play a role in the folding process of lobate scarps (e.g. Klimczak et al., 2018), but a simple fault propagation folding

mechanism has been chosen for modeling simplification purposes. The role of fault propagation folding is strongly supported by the evidence of surface rupture. The fault propagation fold of each lobate scarp forming the Amenthes Rupes fault system has been modeled using the fault parallel flow (Egan et al., 1997; Kane et al., 1997; Wheeler, 1987) and trishear (Allmendinger, 1998; Erslev, 1991) algorithms applied in a 3D modeling framework (Cardozo, 2008; Cristallini & Allmendinger, 2001) using MOVE^{TM} software (Midland Valley). The fault parallel flow algorithm determines the deformation of the hanging wall caused by the displacement over a complex fault geometry, while the trishear method defines the deformation distributed ahead of a propagating tip point. The combination of both algorithms is a pure geometric approach, which was designed for modeling strain in the brittle lithosphere, characterized by faulting and folding assuming volume conservation (e.g. Cristallini & Allmendinger, 2001; Ziesch et al., 2014). This combination, has been proved useful in the modeling of thrust belts on Earth (e.g. Cardozo, 2008; Cardozo & Brandemburg, 2014; Cristallini & Allmendinger, 2001; Li et al., 2020; Maesano et al., 2013; Watkins et al., 2015) to constrain the tectonic scenarios at depth due to the possibility of varying the parameters that define faulting and folding along the structure. It has also been applied to model Ogygis Rupes lobate scarp together with two subsidiary backthrusts (Herrero-Gil et al., 2020) on Mars. The topographic surface of Amenthes Region has been modeled attending to the premise that the erosion rates on Mars have remained low since lobate scarps formation (e.g. Golombek & Phillips, 2010). We have assumed that no other mechanisms has substantially altered the slopes of the structural reliefs identified as the result of the displacement of the underlying thrust fault system, although some gravitational deposits at the scarps bases can be observed at some scarce locations.

Fault parallel flow algorithms constrain the movement of the hanging wall over the footwall through the assumption of volume conservation (Ziesch et al., 2014). The deformation is defined by a fault parallel shear, where the material of the hanging wall moves in the direction of the fault slip along flow paths parallel to the fault surface. The geometry of the fault plane controls the topography of the lobate scarp (Schultz & Watters, 2001; Watters et al., 2002), specifically the dip and depth of the fault plane mostly define the width of the associated lobate scarp (distance between the trailing syncline and the scarp base), and the fault slip controls the relief of the structure. The depth of faulting influences the amount of uplifted material, defining the location of the syncline and consequently the width of the anticline, while the dip angle of the fault is directly related to the slope of the backlimb. Accordingly, variations in fault dip at depth modify the backlimb slope. A gradual decrease of the dip angle at depth, flattening downwards into the decollement (resulting in listric fault geometries) creates a gentle and wider backlimb, due to a tilting of the hanging wall with respect to the footwall (e.g., Amos et al., 2007; Erslev, 1986; Johnson & Johnson, 2002; Ziesch et al., 2014). If the decrease of the dip angle at depth is abrupt, it generates a steeper and narrower backlimb (e.g. Amos et al., 2007; Ziesch et al., 2014). The absence of rooting level, using a fault that ends abruptly, would result in a lack of backlimb development and non-generation of a trailing syncline. The effect in the topography caused by the variation of these fault parameters is explained in Text S1 (Supporting information).

Trishear algorithms (Allmendinger, 1998; Erslev, 1991) successfully replicate the folding ahead of a propagating thrust fault (Fig. 2). In cross section, the folding occurs in a triangular shear zone (trishear zone) defined by a variable angle (θ) (Allmendinger, 1998), where a distributed shear deforms the material ahead of a propagating fault tip. The trishear parameters define the shape of the main anticline and the frontal syncline, through the distribution of the trishear zone between the hanging wall and the footwall (θ_1, θ_2) with respect to the fault

(Zehnder & Allmendinger, 2000), the depth of the initial fault tip, and the fault propagation to fault slip ratio (P/S) (Hardy & Ford, 1997). A small trishear area implies that the deformation is more concentrated, creating a narrower syncline (with a steeper forelimb) than if the deformation is distributed in a larger trishear area (Allmendinger, 1998). The P/S ratio (Hardly and Ford, 1997) is directly related to the degree of fold development. Low P/S values (below 2) imply that the material spends more time in the trishear zone, undergoing more deformation of the forelimb before faulting. The effect that the variation of trishear parameters has on the uplifted topography is explained in Text S1 (Supporting information).

The modeling workflow comprises from the construction of the fault surfaces to the reproduction of the observed topographic surface through the forward slip of the thrust faults with propagating fault tips and associated trishear folding (Herrero-Gil et al., 2020). Firstly, a preliminary 2D restoration of the topographic surface and forward modeling were performed for several cross sections made along each fault, to get a first order approximation of the fault geometries. The 3D fault surfaces used during the modeling were built by interpolation between these cross sections. Secondly, the created 3D fault surfaces were validated thought a 3D restoration of the MOLA observed topographic surface. These 3D fault geometries serve as a starting point for the restoration, and their shapes were modeled until generating the best surface restoration, through the iterative variation of dip and depth along the structure paying attention to the resulting topographic surface modifications (see Text S1 Supporting information). This restoration process shows the subsurface interaction between nearby structures, and provides an approximation for fault slip values and trishear parameters. Finally, the 3D fault geometries resulting from the 3D restoration have been used in the 3D forward modeling. Fault slip and trishear parameters have been adjusted in this last step of the process, comparing the resulting modeled surface to the original MOLA topography until the best possible fit is achieved. The initial topographic surface used during the 3D forward modeling was obtained from the original MOLA topography, from which crater depressions, rims, ejecta and structural reliefs related to lobate scarps were removed (Herrero-Gil et al., 2020), taking the grid points that are outside these structures and interpolating the surface using the kriging geostatistical procedure.

3 3D Structural analysis results

The area of study includes Amenthes Rupes (main fault) and other four major thrust faults forming the largest structural reliefs (Fig. 1, Table 1). The general vergence of these lobate scarps is towards the SW, except for Fault 3 which is a backthrust verging NE. The main fault and faults 2, 3 and 4 are interrelated, their traces intersect or their associated topographies interfere with each other. Otherwise, Fault 5 is located parallel to Amenthes Rupes in the NE of the study area.

3.1 3D Restoration

The restoration of the lobate scarp reliefs present on the observed MOLA topographic surface (Fig. 3a) has been made by reversing the thrust slip of the underlying 3D fault surfaces in order to obtain a surface without any relief associated with thrust faults, which is representative of the topographic surface prior to contractional deformation (Fig. 3b)

The modeled fault surfaces reflect a planar geometry in the upper kilometers with a gradually decrease of the dip at depth, until it flattens when reaching the decollement level, resulting in listric morphologies constrained by the shape of the structural relief. The presence of

a decollement level is supported by the presence of a trailing syncline associated with all the thrust faults modeled (Fig. 1). Subsurface relationships between faults appear when trying to restore MOLA topography, which allows us to group the five studied faults. Each thrust fault has been assumed to present dip-slip reverse faulting with the slip vector of each fault perpendicular to the fault strike, since no evidence of a strike-slip component of deformation was observed.

3.1.1 Main fault and Fault 2

The Amenthes Rupes lobate scarp is generated by a 470 km long thrust fault. The largest relief (~1050 m) of Amenthes Rupes is located near the center of the structure and corresponds with the crest of the fault propagation anticline. The surface rupture of this thrust fault is denoted by a cross-cut crater located approximately in the middle of the structure (Mueller et al., 2014). The modeled dip angle of the main thrust fault is 27º–28º NE for the first ~30–32 km (measured on the fault plane from the surface), until a depth of ~14–15 km, where the dip angle begins a gradually decrease with a listric geometry. The main fault roots into a decollement at 20 km of depth in the northwestern part of the structure, deepening up to 24 km in the southeastern part (Fig. 4b, c).

Fault 2 is a 180 km long thrust fault that entirely overlaps the southern part of the main fault, being mostly parallel to it. It is located on the hanging wall of the main thrust fault, with a spacing value of ~10 km, although it increases up to 20 km near the southeast fault tip. The maximum relief associated with this fault is ~570 m. Fault 2 is modeled as a splay fault that roots with a listric geometry at the same decollement than the main fault (Fig. 4b). However, it presents a slightly higher dip angle than the main fault (29.5º NE) for the upper ~31 km measured on the fault plane from the surface (until ~15 km deep).

3.1.2 Fault 3 and Fault 4

Fault 3 is a 220 km long thrust fault verging NE, opposite to the main fault vergence (i.e. Fault 3 is a backthrust), which presents an arcuate form in map view. Fault 3 intersects at the present topographic level with the main fault at 130 km from its southern tip point, forming a 40 km long pop-up elevation located north of the intersection-point. The main fault and Fault 3 form a pop-down structure southwards from this intersection-point (Fig. 4a, b). The lobate scarp associated with Fault 3 presents a maximum relief of 900 meters in its central part. The dip angle of this backthrust is estimated to be 31º–33º SW for the first ~29 km (measured along the fault from the surface), until ~15 km of depth, where the dip angle decreases gradually in a listric geometry. The depth of faulting has been set at 21.5–22.5 km. Two minor faults, not included in the modeling due to their small dimensions (Fig. 1), seem to distribute the displacement of this fault to the southeast.

Fault 4 is a SW verging thrust fault separated 70 km southeast from Fault 3, striking parallel to it. It is a 126 km long thrust fault that overlaps along all its length with Fault 3, generating a pop up structure (Fig. 4a, b). The backlimb of its associated lobate scarp presents two big craters that mask the morphology of the uplifted relief, which has been measured to be 800 m. The fault surface underlying this structure presents an estimated dip angle of 23º NE for the first ~22 km (measured along fault from the surface) that decreases gradually at ~9 km of depth until rooting at 13 km deep into the subhorizontal decollement (Fig. 4b).

3.1.3 Fault 5

Faults 5 is located ~85 km northeast from the main fault and parallel to it and it is formed by two linked fault segments. The NW Segment presents a linear trace 180 km long. The topography of the anticline forming the lobate scarp was modified by impact craters, but its maximum relief has been measured to be 600 m. The SE segment is 160 km long, and it is separated ~15 km south from NW Segment, overlapping 25 km. Its trace reflects two lobes in map view, with a maximum relief peak in each lobe of approximately 500 meters. Both fault segments present similar modeled dip angles (27º–28º NE) near the surface (the first ~15–16 km measured on the fault plane) decreasing from ~7–8 km of depth. The depth of faulting of Segment NW is calculated to be 10.5–11.5 km (Fig. 4e), while the SE Segment roots at 9.5–11 km.

3.2 3D Forward modeling

The 3D forward modeling reproduces the original topographic surface (Fig. 3a) starting with the fault surfaces obtained from the 3D restoration to deform an initial surface in which the uplifted topography related to the displacement of the thrust faults have been removed (Fig. 5a). The best fit model (Fig. 5b) is obtained modeling the fault propagation fold for each thrust fault along its strike, by adjusting the trishear parameters that define the folding ahead of the propagating fault tip (Table 1) and the distribution of the fault slip (Fig. 6).

Main thrust fault, Fault 2, the backthrust (Fault 3) and the NW Segment of Fault 5 present large modeled trishear angles (80º–86º), while Fault 4 and the SE Segment of Fault 5 present moderate trishear angles (44º–60º). The P/S ratios for the main fault and Fault 3 have been estimated to be 3, however the P/S ratios obtained for the other faults included in the model are 2.

The distribution of the cumulative fault slip (Fig. 6) calculated for each analyzed thrust fault reflects a decay of the slip towards the lateral tip points. The maximum slip is located in the center of the main fault, with an estimated value of ~2100 m that towards the northwest decay to zero while in the southeast flattens out at ~1050 m before the decreasing. Fault 2 presents a symmetric peak type slip distribution (Fossen, 2010) with a maximum modeled slip of ~1300 m in the center that coincides with the secondary flat top of the main fault. The maximum fault slip of Fault 3 is estimated to be ~1600 m, and it is located approximately 75 km from its southern tip point leading to an asymmetric slip distribution. This fault presents a constant decrease to zero slip towards the south, while to the northern tip point the slip decreasing plummets when it intersects with the main fault. Fault 4 presents a symmetric plateau type slip distribution (Fossen, 2010) with a maximum flat top corresponding with an estimated slip of ~1720 m. The maximum modeled slip of Fault 5 NW Segment is ~1100 m, which is located at 30 km from the southeastern tip point. The modeling of the SE Segment of Fault 5 reflects two peaks in the slip distribution of ~1000 and ~920 m corresponding with the two lobes identified in plan view (Fig.1).

The accuracy of the best fit model obtained has been probed by comparison with the observed MOLA topography (Fig. 7), trying to minimize the elevation difference between them. The study area is characterized by the presence of a large number of impact craters that modify the topography. The greatest differences in elevation are due to these impact craters that we have removed from the initial modeling surface when removing the lobate scarp reliefs, thus the

calculation of the difference between the observed topography (Fig. 3a) and the forward modeled topography (Fig. 5b) has been made excluding crater values. The median value calculated for the elevation difference between the MOLA model and the modeled topographic surface is ~3 m. The quartile deviation associated with this median value, which is indicative of the average fit of the model, is ~29 m, indicating that half of the values obtained when comparing these two surfaces are concentrated between 32 m and -26 m.

4 Discussion

4.1 Structural modeling

The general agreement of the forward modeled topographic surface and the MOLA observed surface (Fig. 7) is evidenced by the low median value (~3) and the dispersion of the data around it (quartile deviation of ~29 m). This quartile deviation represents 2.8% of the maximum relief associated with the main fault (1050 m), while it represents 6% of the maximum relief associated with the smallest modeled fault (Fault 5 Segment SE, 480 m). The uncertainties in the fault slip estimate that can cause the obtained quartile deviation of the modeled topography (29 m) are +/- 74 m for a the minimum modeled dip angle (23º) and +/- 53 m for the maximum modeled dip angle (33º) (the slip uncertainty can be obtained by the quartile deviation / sin β, being β the dip angle). These values show that our 3D model is a good approximation to the geometry and kinematics of thrust faults in the study area, which closely reproduces lobate scarp structural reliefs, nevertheless this model is a simplification, and some minor local differences can be observed due to modeling limitations and non-modeled geological processes.

The modeling method presents some limitations when the propagating fault reaches the topographic surface (surface rupture). The trishear fault propagating folding ends at this point and the hanging wall continues its displacement over the footwall following a fault parallel flow movement. This, together with the presence of landslides and rockfalls due to the steep slope of the forelimb, hinder to fit the forelimb and the scarp base throughout the entire length of the structure, generating small misfits between the model and the original surface especially at the scarp bases. The building of the 3D fault planes has been performed idealizing them as a smooth surfaces, therefore the presence of probable irregularities along fault surfaces, which would influence the topography (Watkins et al., 2015), have not been taken into account. From this point of view, our model can be considered a first order approximation to the general 3D faulting framework. The tectonic transport direction has been set perpendicular to each fault strike, although Mueller et al. (2014) obtained a slip vector direction for Amenthes Rupes that deviates 16º from pure dip-slip, by measuring the dislocation of a crater cut by the main fault, which would reflect a small strike-slip component of deformation. However, these authors claim that this estimate presents a significant error, because the half of the crater located on the hanging wall is affected by a subsequent crater, significantly reducing the amount of data involved in the calculation. Besides, an oblique slip generates surface geometries similar to those generated by dip-slip (Cristallini & Allmendinger, 2001), and an obliquity of the slip as low as 16º only results in a very slight changes in slip and trishear angle needed to fit the model. A pure dip-slip fault kinematics has been assumed for all the modeled faults with the slip vectors perpendicular to the average strike of fault traces, because the high sinuosity of the mapped lobate scarps (Fig. 1) and the lack of en-echelon patterns does not indicate an evident strike-slip component of deformation.

The fault surfaces obtained in this study for the five analyzed faults show positive listric morphologies at depth (a decay of dip angle with depth, McClay and Ellis, 1987). Previous studies using the FMD method modeled the underlying fault of Amenthes Rupes, as well as other lobate scarps in Mars, as a rectangular planar fault (Egea-González et al., 2017; Herrero-Gil et al., 2019; Grott et al., 2007; Ruiz et al., 2008; Schultz & Watters, 2001), because this method does not provide results as good as when the model is made using non-planar morphologies (Schultz & Watters, 2001; Watters & Nimmo, 2010). A positive listric fault morphology was obtained by Mueller et al., (2014) for Amenthes Rupes and by Herrero-Gil et al., (2020) for Ogygis Rupes and its backthrusts, based on the relation between the fault propagation anticline topography and the fault plane characteristics (e.g. Amos et al., 2007; Cardozo & Brandemburg, 2014; Ellis et al., 2004; Erslev, 1986; Seeber & Sorlien, 2000). On the contrary, a planar fault morphology that keeps its dip constant until the horizontal decollement would generate a backlimb with the same dip as the fault and abrupt limits (e.g. Amos et al., 2007; Brandemburg, 2013; Hardy & Ford, 1997), which is not the case for any of the studied faults (Supporting information Figure S1).

The dip angles obtained for the first kilometers of depth for the analyzed faults range between 27º and 33º (Table 1), except Fault 4 which presents a lower dip angle of 23º. These dip values are within the typical range calculated for reverse faults (20–35º) (e.g., Jaeger & Cook, 1979; Stone, 1985; Watters & Nimmo, 2010). The lower dip of Fault 4 can be explained by considering its relation with Fault 3 (Fig. 4). Both faults form a "pop up" structure in which Fault 4 roots at a shallower depth indicating that it is subsidiary. Fault 4 can be passively transported by Fault 3 with a slight tilting due to its listric fault morphology at depth, causing the decreasing of its dip angle as Fault 3 slips (Ellis et al., 2004).

The estimated slip distribution (Fig. 6) of the studied fault set, allows us to obtain an approximate value of the horizontal shortening in the area (Fig. 8) as a result of the NE-SW compressive stress that generated these structures. The listric geometry obtained for these faults at depth suggests that the slip on the fault ramps near the surface was transmitted by a horizontal slip of the same value along the decollement (Herrero-Gil et al., 2020). Thereby, the regional shortening related to Amenthes Rupes thrust fault system can be estimated by stacking the slips of the contractional faults in the area (Fig. 8). This value has been measured in the direction N36.6ºE, the mean dip azimuth of the studied faults (Fig. 4d) which is orthogonal to the mean strike value. The horizontal displacement presents a multimodal asymmetrical distribution characterized by 3 peaks of different value increasing notably towards the southeast. The northwestern peak is due to the contraction accommodated by the NW part of the main fault and the NW Segment of Fault 5. The horizontal slip corresponding to the central peak is due to the shortening generated by the slip of the central part of the main fault and the SE Segment of Fault 5. The southeastern peak shows the largest shortening value of the total distribution (~5450 m) due to the combining of the slip values generated by faults 2, 3, 4 and the southern part of the main fault, which are mostly parallel in this area (Fig. 1). The analysis of the shortening distribution (Fig. 8) shows a main change in the amount of shortening at ~360 km from the NE. This point marks an abrupt increase of shortening towards the SE associated with the third described peak. The structural map (Fig. 1) reveals that faults 2, 3 and 4 appear to the SE of this diffuse limit, where Fault 5 ends. The largest shortening value abruptly decays to the southeast. In this area there are two minor faults (Fig. 1) not included in the modeling that distribute the slip of the Fault 3 to the south. These minor faults seem to have a shorter length due to the presence of a heavily cratered area affecting their traces (southeast corner Fig. 1), nevertheless these

structures continue to the S-SE outside the study area with associated high relief, which reflects that the shortening continues along these faults although they are not included in this study.

Therefore, the shortening associated with each fault is equal to the fault slip under the assumption that the slip is transmitted from the decollement due to the listric fault morphology at depth. This interpretation requires that the shortening estimates calculated using listric fault morphologies are larger than when the shortening is obtained from the horizontal component of the slip (heave) over a planar fault (from ~6% for a dip angle of 20º, up to ~30% for 40º) (Herrero-Gil et al., 2020). Consequently, the horizontal contraction that generated lobate scarps implies a shortening value up to ~30% larger than the estimates calculated from modeling the slip over a planar fault.

The analysis of the calculated faulting depths presents a bimodal distribution, so, the obtained results can be grouped in two different depths (Table 1). The major faults of the area (the main fault, its splay Fault 2, and Fault 3), which are the longest, and uplift the widest and highest reliefs, root in a deep decollement level, that ranges in depth from 20–24 km. This depth value is within the range of depths of faulting calculated previously for the large faults underlying different lobate scarps formed in the Late Noachian/Early Hesperian spread across the highlands of Mars (Egea-González et al., 2017; Grott et al., 2007; Herrero-Gil et al., 2019, 2020; Mueller et al., 2014; Ruiz et al., 2008; Schultz & Watters, 2001), supporting that this rooting level is not a regional rheological threshold. The depth of faulting of these large thrust faults has been considered as the BDT depth at the time of its formation (e.g. Ruiz et al., 2008, 2009, 2011; Schultz & Watters, 2001), which corresponds to a change from localized failure to distributed failure (Byerlee, 1967, 1968; Rutter, 1986). On the other hand, Fault 4 and the two segments corresponding to Fault 5 present a modeled depth of faulting of 11–13 km, much shallower than the BDT where the large faults root. This bimodal distribution of depths shows the mechanical complexity of the crustal layers affected by faulting, indicating that the lithospheric brittle domain is not a homogeneous medium, but it probably presents heterogeneities such as mechanical discontinuities where subsidiary faults root.

The results obtained in this study for the major faults in the area that root in a deep decollement (main fault forming Amenthes Rupes, Fault 2 and Fault 3) can be compared with the fault parameters estimates of previous works in Amenthes Rupes, which are focused in the main fault (Egea-González et al., 2017; Mueller et al., 2014; Ruiz et al., 2008; Schultz & Watters, 2001) (Table 2). The slip value calculated for the main fault is within the range calculated by Ruiz et al., (2008), while is quite higher than the values calculated by other authors (Egea-González et al., 2017; Mueller et al., 2014; Schultz & Watters, 2001). Fault 2 and Fault 3 are expected to present different slip values since they are different structures than the main fault. However, the depth of faulting of these faults in the area can be compared because it is expected that the BDT does not present large variations in such a small area during the same period of time. When we compare the depths of faulting of these 3 faults with previous works (Egea-González et al., 2017; Mueller et al., 2014; Ruiz et al., 2008; Schultz & Watters, 2001), our estimates provide shallower values. The BDT is temperature and strain rate dependent (e.g. Artemieva, 2011; Ruiz et al, 2011). The shallower depth of the BDT deduced from our results suggests that the associated heat flow of the Amenthes Region at the time of lobate scarps formation could be somewhat higher than previous estimates. Faster deformation deepens the brittle domain of the crust. The strain rates calculated for the Amenthes thrust fault system (Schultz, 2003) are small (between 10^{-17} and 10^{-19} s^{-1}) and comparable to intraplate tectonic

settings on Earth; accordingly, large variations in the strain rate, affecting significantly the depth of the BDT, are not expected in this area. The dip values obtained are in the range of those previously calculated for Amenthes Rupes (19º–35º) (Egea-González et al., 2017; Ruiz et al., 2008; Schultz & Watters, 2001), but away from the highest values obtained by Mueller et al., (2014).

The trishear parameters obtained for the modeled faults (Table 1) are within the best-fit ranges calculated by Pei et al. (2014) through the analysis by trishear of several real structures on Earth. They stablished a P/S ratios ranging between 2 and 3 and trishear angles between 30º and 100º. The main fault and Fault 3 present a P/S ratio of 3, coinciding with their larger dimensions and deeper depths of faulting. They also have in common a large trishear angle (80º–86º) showing that the folding occurs in a wide area that in main fault affects mainly the hanging wall, while in Fault 3 equally affects the hanging wall and the footwall. Fault 2 presents a trishear angle and its distribution similar to the main fault (Fault 2 is a splay of the main fault), with a P/S ratio of 2. Fault 4 and both segments of Fault 5 also have P/S ratios of 2, and variable trishear angles between 40º and 85º. The initial fault tip depth of SE Segment of Fault 5, comparing to its maximum slip, reflects that this fault does not break the topographic surface at the end of the forward modeling. The fault propagation is strongly linked with the fault slip distribution. This may imply that the surface rupture does not occur along the structure (blind thrust), or that it occurs at specific locations that usually match with the location of maxima in the slip distribution.

The modeling of Fault 4 presented several challenges. The propagating fault tip of this fault at the end of the forward modeling does not reach the topographic surface, suggesting that this could be a blind fault. However, the large original topographic dimensions of this fault and its net scarp base observed in the MOLA topography and THEMIS images suggest a surface rupture at least in its central part. The scarp base and frontal syncline generated by Fault 4 displacement are completely covered by a deposit of Amazonian-Hesperian smooth plains (Erkeling et al., 2011). Caprarelli et al. (2007) estimated the thickness of this geological unit by calculating the depth of the craters before the infilling. The high thickness of this resurfacing material (1–1.5 km) suggests that the relief uplifted by Fault 4 was initially much higher than the relief currently observed. Moreover, the backlimb Fault 4 propagation anticline is affected by two big impact craters postdating the fault displacement and by the presence of some wrinkle ridges (Fig. 1) parallel to Fault 3 and 4, which also affect the modeling results. These two large craters were also infilled by the same resurfacing unit. Therefore, the obtained slip for this fault is a minimum value and due to these observations other parameters of Fault 4 may also present additional uncertainties.

4.2 Tectonic evolution and implications for global contraction

Since Amenthes Rupes and its companion thrust faults are located in the highlands near the dichotomy boundary, their characteristics can give us information on the evolution of the boundary, at least locally. The faults forming the Amenthes Region thrust fault system all show similar strikes and kinematics (pure reverse faults), thus can be interpreted to be formed under the same compressive stress field with a shortening direction (N36.6ºE) perpendicular to their average strike (Fig. 4d). This agrees with the direction of the dichotomy boundary and with other lobate scarps in the adjoining Arabia Terra and Terra Cimmeria (Nimmo, 2005; Watters, 2003a; Watters & Robinson, 1999; Watters et al., 2007).

Watters and Robinson (1999) calculated the horizontal shortening across Amenthes Rupes using the fault throw (lobate scarp relief), obtaining 1800–3400 m (corresponding with the heave on a planar fault), depending on the dip angle (assumed to be 20º–35º). The fault parameters obtained in the present 3D modeling also allow a constraint on the maximum shortening registered by Amenthes Rupes main fault, which is ~2100 m, assuming that the slip is transmitted from the decollement. The regional shortening distribution associated with the whole fault system (Fig. 8) suggests a maximum value in the southeastern of the thrust system of ~5450 m which is well above the previously calculated range for this area (1800–3400 m), increasing the shortening estimates of the area between ~60 and ~200%. This difference in the shortening values is mainly due to the inclusion of secondary and subsidiary faults in our model that were not previously considered, and yet they accommodate ~62% of the maximum shortening in this area. Besides, there are other minor contractional structures identified in the area (Fig. 1), including minor thrust faults and wrinkle ridges, that have not been included in the model and they would increase this shortening calculation, especially in the southeastern half of the thrust fault system. Whereby the regional shortening estimated by our model (Fig. 8) is a minimum value. Previous global shortening estimates based on thrust faults (Nahm & Schultz, 2011) were performed using the dataset of faults of Knapmeyer et al., (2006). Although this structural mapping is quite exhaustive and extensive, the number of structures considered were significantly biased by the global scale of mapping, so the database did not contain all the subsidiary and minor faults present on Mars surface. Our study shows that the consideration of subsidiary faults, including backthrusts and fault splays, and independent secondary and minor faults in global calculations of contraction, would provide a significant increase of the global planetary shortening accommodated by thrust faulting.

Although all the faults were generated during the same epoch, some relative time relationships can be deduced from structural cross-cut evidence, providing information on the evolution of the fault system. Fault 2 is a splay of the main fault indicating that the slip of main fault is progressively accommodated by Fault 2 towards the SE. This kinematic link between both faults, which root at the same decollement, suggests that they could have been active at the same time. The main fault and Fault 2 traces are slightly displaced by Fault 3 slip, indicating that, although the activity of these faults could be contemporary, the last movement belongs to Fault 3 (backthrust). Fault 4 is a subsidiary antithetic fault with respect to Fault 3, consequently both faults are probably contemporary. Fault 5 does not intersect other faults so it is not possible to deduce its place in the formation order.

A general tectonic evolution of the contraction that generated the lobate scarps in the Amenthes Region can be outlined according to the described cross-cutting constraints and the horizontal slip distribution of Fig. 8. Initially, the compressional stress field generated a homogeneous shortening in the area associated with the main fault, Fault 2 and probably Fault 5. Later, the contraction continued in the SE region of the study area with the generation of Fault 3 and its subsidiary Fault 4 which significantly increases the total shortening in this sector (maximum peak shown in Fig. 8), propagating deformation towards the SW with respect to the main fault and its splay (Fig. 1). This assumption that the deformation shifts and continues to the southeast agrees with previous observations that the lobate scarps on Terra Cimmeria, located ~500 km southeast of the studied fault system, deform geological units from the early Hesperian, which indicates that their formation continued during that age (Greeley & Guest, 1987; Watters & Robinson, 1999; Watters et al., 2007). These observations can be representative of the evolution pattern of the deformation that modified this part of the dichotomy boundary in the

Late Noachian/Early Hesperian, which implies a shortening recorded by thrust faults that is more than double of previous estimates if the calculation includes subsidiary and secondary faults.

5 Conclusions

Five thrust faults forming the Amenthes thrust fault system, which is located in the Amenthes Region, have been modeled though a combination of trishear and fault parallel flow by 3D forward modeling. All the modeled fault surfaces show listric geometries at depth constrained by the low slopes of the fault propagation anticline backlimbs and by the width of the trailing syncline. The obtained depths of faulting of the major faults present in the fault system suggest a depth of the BDT of 20–24 km at the time of formation in the Late Noachian/Early Hesperian, a value shallower than previous estimates. A possible mechanical discontinuity in the lithosphere located at 10.5–13 km of depth can be deduced from the depths of faulting of secondary faults. The estimated horizontal shortening accumulated by the thrust system ranges between 2000 and 3000 m, increasing towards the SE part of the study area to a maximum shortening value of ~5450 m. This value represents an increase in the maximum regional shortening registered by thrust faults of between 60 and 200% higher than previous estimates, due to the consideration of subsidiary and secondary faults. The contribution of minor, secondary and subsidiary faults to the planetary contraction could provide a significant increase of martian global shortening.

Acknowledgments

This research has been supported by the project AMARTE2 PR75/18-21613, funded by the research program Santander-UCM, and TECTOMARS PGC2018-095340-B-I00, funded by the Spanish Ministry of Science, Innovation and Universities. A. Herrero-Gil work has been supported by a FPI2015 grant BES-2015-073983, funded by the Spanish Ministry of Economy and Competitiveness (MINECO). The software MOVE 2018.2 was provided by Petroleum Experts Ltd. through the donation of an Academic license to the Departamento de Geodinámica, Estratigrafía y Paleontología, Universidad Complutense de Madrid. The authors thank V. Galluzzi, R. Knipe and the editor L. Montesi for their helpful reviews, which have improved the quality of the manuscript. The data used in this research are available online at the NASA Planetary Data System. The resulting data presented in this manuscript are publicly available at https://doi.org/10.6084/m9.figshare.10596530

References

Allmendinger, R. (1998). Inverse and forward numerical modeling of trishear fault-propagation folds. Tectonics, 17 (4), 640–656.

Amos, C. B., Burbank, D. W., Nobes, D. C., & Read, S. A. (2007). Geomorphic constraints on listric thrust faulting: Implications for active deformation in the Mackenzie Basin, South Island, New Zealand. Journal of Geophysical Research, 112, B03S11.

Anguita, F., Fernández, C., Cordero, G., Carrasquilla, S., Anguita, J., Núñez, A., et al. (2006). Evidences for a Noachian-Hesperian orogeny in Mars. Icarus, 185, 331-357.

Brandenburg, J. P. (2013). Trishear for curved faults. Journal of Structural Geology, 53, 80–94.

Byerlee, J. D. (1967). Frictional characteristics of granite under high confining pressure, Journal of Geophysical Research, 72, 3639–3648.

Byerlee, J. D. (1968), Brittle ductile transition in rock. Journal of Geophysical Research, 73, 4741–4650.

Byrne, P. K., Klimczak, C., McGovern, P. J., Mazarico, E., James, P. B., Neumann, G. A., et al. (2015). Deep-seated thrust faults bound the Mare Crisium lunar mascon. Earth and Planetary Science Letters, 427, 183-190.

Caprarelli, G., Pondrelli, M., Di Lorenzo, S., Marinangeli, L., Ori, G. G., Greeley, R., & Neukum, G. (2007). A description of surface features in north Tyrrhena Terra, Mars: Evidence for extension and lava flooding. Icarus, 191, 524–544.

Cardozo, N. (2008). Trishear in 3-D: Algorithms, implementations and limitations. Journal of Structural Geology, 30, 327–340.

Cardozo, N., & Brandenburg, J. P. (2014). Kinematic modeling of folding above listric propagating thrusts. Journal of Structural Geology, 60, 1–12.

Chamberlin, R. T. (1910). The Appalachian folds of central Pennsylvania. Journal of Geology, 18, 228-251.

Chamberlin, R. T. (1919). The building of the Colorado Rockies. Journal of Geology, 27, 225–251.

Christensen, P., Jakosky, B. M., Kieffer, H. H., Malin, M. C., McSween, H. Y. Jr., Nealson, K., et al. (2004). The Thermal Emission Imaging System (THEMIS) for the Mars 2001 Odyssey mission. Space Science Reviews, 110, 85–130.

Crane, K. T., & Klimczak, C. (2019). Tectonic Patterns of Shortening Landforms in Mercury's Northern Smooth Plains. Icarus, 317, 66–80.

Cristallini, E. O., & Allmendinger, R. W. (2001). Pseudo 3-D modeling of trishear fault-propagation folding: Journal of Structural Geology, 23, 1883–1899.

Dahlstrom, C. D. A. (1969). Balanced Cross Sections. Canadian Journal of Earth Sciences, 6 (4), 743–757.

Egan, S. S., Buddin, T. S., Kane, S. J., & Williams, G. D. (1997). Three-dimensional modelling and visualization in structural geology: New techniques for the restoration and balancing of volumes. Proceedings of the 1996 Geoscience Information Group Conference on Geological Visualization. Electronic Geology, 1, 67–82.

Egea-González, I., Jiménez-Díaz, A., Parro, L. M., Lopez, V., Williams, J. P., & Ruiz, J. (2017). Thrust fault modeling and Late-Noachian lithospheric structure of the circum-Hellas region, Mars. Icarus, 288, 53–68.

Egea-González, I., Ruiz, J., Fernández, C., Williams, J. P., Márquez, A., & Lara, L. M. (2012). Depth of faulting and ancient heat flows in the Kuiper region of Mercury from lobate scarp topography. Planetary and Space Science, 60, 193–198.

Ellis, S., Schreurs, G., & Panien, M. (2004). Comparisons between analogue and numerical models of thrust wedge development. Journal of Structural Geology, 26, 1659–1675.

667 Erkeling, G., Hiesinger, H., Reiss, D., Hielscher, F. J., & Ivanov, M. A. (2011). The stratigraphy
668 of the Amenthes region, Mars: Time limits for the formation of fluvial, volcanic and
669 tectonic landforms. Icarus, 215, 128–152.

670 Erslev, E. A. (1986). Basement balancing of Rocky Mountain foreland uplifts. Geology, 14,
671 259–262.

672 Erslev, E. A. (1991). Trishear fault-propagation folding. Geology, 19, 617–620.

673 Fossen, H. (2010). Structural Geology. 1st edition, Cambridge University Press, Cambridge, UK.

674 Galluzzi, V., Achille, G. D., Ferranti, L., Popa, C., & Palumbo, P. (2015). Faulted craters as
675 indicators for thrust motions on Mercury. Geological Society Special Publication, 401,
676 313–325.

677 Galluzzi, V., Ferranti, L., Massironi, M., Giacomini, L., Guzzetta, L., & Palumbo, P. (2019).
678 Structural analysis of the Victoria quadrangle fault systems on Mercury: Timing,
679 geometries, kinematics, and relationship with the high-Mg region. Journal of Geophysical
680 Research: Planets, 124, 2543–2562.

681 Giacomini, L., Massironi, M., Galluzzi, V., Ferrari, S., & Palumbo, P. (2019). Dating long thrust
682 systems on Mercury: New clues on the thermal evolution of the planet. Geoscience
683 Frontiers, in press. https://doi.org/10.1016/j.gsf.2019.09.005

684 Golombek, M. P., & Bridges, N. T. (2000). Erosion rates on Mars and implications for cli- mate
685 change: constraints from the Pathfinder landing site. Journal of Geophysical Research,
686 105 (E1), 1841–1853.

687 Golombek, M. P., & Phillips, R. J. (2010). Mars tectonics. In: Planetary Tectonics. Cambridge
688 University Press, Cambridge, UK. 183–232.

689 Greeley, R., & Guest, J. E. (1987). Geologic map of the eastern equatorial region of Mars, scale
690 1:15,000,000, U.S. Geological Survey Information Services Map, I-1802-B.

691 Grott, M., Hauber, E., Werner, S. C., Kronberg, P., & Neukum, G. (2007). Mechanical modeling
692 of thrust faults in the Thaumasia region, Mars, and implications for the Noachian heat
693 flux. Icarus, 186, 517–526.

694 Hardy, S., & Ford, M. (1997). Numerical modeling of trishear fault propagation folding.
695 Tectonics, 16 (5), 841–854.

696 Herrero-Gil, A., Egea-González, I., Ruiz, J., & Romeo, I. (2019). Structural modeling of lobate
697 scarps in the NW margin of Argyre impact basin, Mars. Icarus, 319, 367–380.

698 Herrero-Gil, A., Ruiz, J., & Romeo, I. (2020). 3D modeling of planetary lobate scarps: The case
699 of Ogygis Rupes, Mars. Earth and Planetary Science Letters, 532, 116004.

700 Jaeger, J. C., & Cook, N. G. W. (1979). Fundamentals of Rock Mechanics, third edition.
701 Chapman and Hall, New York.

702 Jamison, W. R. (1987). Geometric analysis of fold development in overthrust terranes. Journal of
703 Structural Geology, 9 (2), 207–219.

704 Johnson, K. M., & Johnson, A. M. (2002). Mechanical models of trishear-like folds. Journal of
705 Structural Geology, 24 (2), 277–287.

Kane, S. J., Williams, G. D., Buddin, T. S., Egan, S. S., & Hodgetts, D. (1997). Flexural-slip based restoration in 3D, a new approach. American Association of Petroleum Geologists Annual Convention Official Program A58.

Klimczak, C., Kling, C. L., & Byrne P. K. (2018). Topographic Expressions of Large Thrust Faults on Mars. Journal of Geophysical Research: Planets, 123, 1973–1995.

Knapmeyer, M., Oberst, J., Hauber, E., Wählisch, M., Deuchler, C., & Wagner, R. (2006). Working models for spatial distribution and level of Mars' seismicity. Journal of Geophysical Research, 111, E11006.

Li, Z., Chen, W., Jia, D., Sun, C., Zheng, W., Zhang, P., et al. (2020). The effects of fault geometry and kinematic parameters on 3D fold morphology: Insights from 3D geometric models and comparison with the Dushanzi anticline, China. Tectonics, 39, e2019TC005713.

Maesano, F. E., Toscani, G., Burrato, P., Mirabella, F., D'Ambrogi, C., & Basili, R. (2013). Deriving thrust fault slip rates from geological modeling: Examples from the Marche coastal and offshore contraction belt, Northern Apennines, Italy. Marine and Petroleum Geology, 42, 122–134.

Malin, M.C., Bell III, J.F., Cantor, B.A., Caplinger, M.A., Calvin, W.M., Clancy, R.T., et al. (2007). Context Camera Investigation on board the Mars Reconnaissance Orbiter. Journal of Geophysical Research, 112, E05S04.

McClay, K. R., & Ellis, P. G. (1987). Analogue models of extensional fault geometries. Geological Society, London, Special Publications, 28, 109–125.

McGill, G. E., & Dimitriou, A. M. (1990). Origin of the Martian global dichotomy by crustal thinning in the Late Noachian or Early Hesperian. Journal of Geophysical Research, 95, 12595–12605.

Mueller, K., Vidal, A., Robbins, S., Golombek, M., & West, C. (2014). Fault and fold growth of the Amenthes uplift: implications for Late Noachian crustal rheology and heat flow on Mars. Earth and Planetary Science Letters, 408, 100–109.

Nahm, A.L., & Schultz, R.A. (2011). Magnitude of global contraction on Mars from analysis of surface faults: Implications for Martian thermal history. Icarus, 211, 389–400.

Nimmo, F. (2005). Tectonic consequences of Martian dichotomy modification by lower-crustal flow and erosion. Geology, 33 (7), 533–536.

Pei, Y., Paton, D. A., & Knipe, R. J. (2014). Defining a 3-dimensional trishear parameter space to understand the temporal evolution of fault propagation folds. Journal of Structural Geology, 66, 284–297.

Ruiz, J., Fernandez, C., Gomez-Ortiz, D., Dohm, J. M., Lopez, V., & Tejero, R. (2008). Ancient heat flow, crustal thickness, and lithospheric mantle rheology in the Amenthes Region, Mars. Earth and Planetary Science Letters, 270, 1–12.

Ruiz, J., McGovern, P. J., Jiménez-Díaz, A., López, V., Williams, J. P., Hahn, B. C., & Tejero, R. (2011). The thermal evolution of Mars as constrained by paleo-heat flows. Icarus, 215, 508–517.

Ruiz, J., Williams, J. P., Dohm, J. M., Fernández, C., & López, V. (2009). Ancient heat flows and crustal thickness at Warrego rise, Thaumasia Highlands, Mars: Implications for a stratified crust. Icarus, 203, 47-57.

Ruiz, J., Jiménez-Díaz, A., Mansilla, F., Parro, L.M., Egea-González, I, Küppers, M. (2019). Evidence of thrust faulting and widespread contraction of Ceres. Nature Astronomy 3, 916–921.

Ruj, T., Komatsu, G., Pondrelli, M., Di Pietro, I., & Pozzobon, R. (2018). Morphometric analysis of a Hesperian aged Martian lobate scarp using high-resolution data. Journal of Structural Geology, 113, 1–9.

Rutter, E.H. (1986). On the nomenclature of mode of failure transitions in rocks. Tectonophysics, 122, 3–4, 381–387.

Schultz, R. A. (2000). Localization of bedding plane slip and backthrust faults above blind thrust faults: Keys to wrinkle ridge structure. Journal of Geophysical Research, 105, E5, 12035–12052.

Schultz, R. A. (2003). Seismotectonics of the Amenthes Rupes thrust fault population, Mars. Geophysical Research Letters, 30, 1303.

Schultz, R. A., & Watters, T. R. (2001). Forward mechanical modeling of the Amenthes Rupes thrust fault on Mars. Geophysical Research Letters, 28, 4659–4662.

Seeber, L., & Sorlien, C. (2000). Listric thrusts in the western Transverse Ranges, California. Geological Society of America Bulletin, 112, 1067–1079.

Semenzato, A., Massironi, M., Pozzobon, R., Galluzzi, V., Rothery, D. A., Ferrari, S. (2018). Discovering Rembrandt basin's subsurface and Enterprise Rupes: 3D-model based on stratigraphic mapping and structural analysis. EPSC Abstracts, Vol. 12, EPSC2018-344.

Smith, D. E., Zuber, M. T., Frey, H. V., Garvin, J.B., Head, J. W., Muhleman, D. O., et al. (2001). Mars Orbiter Laser Altimeter - Experiment summary after the first year of global mapping of Mars. Journal of Geophysical Research, 106 (E10), 23689–23722.

Stone, D. S. (1985). Geologic interpretation of seismic profiles, Big Horn Basin, Wyoming, Part I: East Flank. In Seismic Exploration of the Rocky Mountain Region, edited by R. R. Gries and R. C. Dyer, Rocky Mountain Association of Geologists, Denver, Colorado.

Strom, R. G., Trask, N. J., & Guest, J. E. (1975). Tectonism and volcanism on Mercury. Journal of Geophysical Research, 80, 2478–2507.

Toda, S., Stein, R. S., Reasenberg, P. A., Dieterich, J. H., & Yoshida, A. (1998). Stress transferred by the 1995 Mw=6.9 Kobe, Japan, shock: Effect on after- shocks and future earthquake probabilities. Journal of Geophysical Research, 103, 24543–24565.

Toda, S., Stein, R. S., Richards-Dinger, K., & Bozkurt, S. (2005). Forecasting the evolution of seismicity in southern California: Animations built on earthquake stress transfer. Journal of Geophysical Research, 110, B05S16.

Watkins, H., Butler, R. W. H., Bond, C. E., & Healy, D. (2015). Influence of structural position on fracture networks in the Torridon Group, Achnashellach fold and thrust belt, NW Scotland. Journal of Structural Geology, 74, 64–80.

Watters, T. R. (2003a). Lithospheric flexure and the origin of the dichotomy boundary on Mars. Geology, 31, 271–274.

Watters, T.R. (2003b). Thrust faults along the dichotomy boundary in the eastern hemisphere of Mars. Journal of Geophysical Research, 108, 5054.

Watters, T.R., & Nimmo, F. (2010). The tectonics of Mercury. In: Planetary Tectonics. Cambridge University Press, Cambridge, UK.

Watters, T.R., & Robinson, M. S. (1999). Lobate Scarps and the Martian crustal dichotomy. Journal of Geophysical Research, 104, 18981–18990.

Watters, T. R., Schultz, R. A., & Robinson, M. S. (2000). Displacement-length relations of thrust faults associated with lobate scarps on Mercury and Mars: Comparison with terrestrial faults, Geophysical Research Letters, 27, 3659–3662.

Watters, T. R., Schultz, R. A., Robinson, M. S., & Cook, A. C., (2002). The mechanical and thermal structure of Mercury's early lithosphere. Geophysical Research Letters, 29, 37–1.

Watters, T. R., & McGovern, P.J, (2006). Lithospheric flexure and the evolution of the dichotomy boundary on Mars. Geophysical Reseach Letters, 33, L08S05.

Watters, T. R., McGovern, P.J., & Irwin III, R. P. (2007). Hemispheres Apart: The Crustal Dichotomy on Mars. Annual Review of Earth and Planetary Sciences, 35, 621–652.

Watters, T. R., Thomas, P. C., & Robinson, M. S. (2011). Thrust faults and near-surface strength of asteroid 433 Eros. Geophysical Research Letters, 38, L02202.

Wheeler J. (1987). Variable-heave models of deformation above listric normal faults: the importance of area conservation. Journal of Structural Geology, 9 (8), 1047–1049.

Wichman, R. W., & Schultz, P. H. (1989). Sequence and mechanisms of deformation around the Hellas and Isidis Impact Basins on Mars. Journal of Geophysical Research, 94, 17333–17357.

Wickham, J. (1995). Fault displacement-gradient folds and the structure at Lost Hills, California (U.S.A.). Journal of Structural Geology, 17 (9), 1293–1302.

Williams, N. R., Watters, T. R., Pritchard, M. E., Banks, M. E., & Bell, J. F. (2013). Fault dislocation modeled structure of lobate scarps from Lunar Reconnaissance Orbiter Camera digital terrain models. Journal of Geophysical Research: Planets. 118, 224–233.

Zehnder, A. T., & Allmendinger, R. W. (2000). Velocity field for the trishear model. Journal of Structural Geology, 22, 1009–1014.

Ziesch, J., Tanner, D. C., & Krawczyk, C. M. (2014). Strain associated with the Fault-Parallel Flow algorithm during kinematic fault displacement. Mathematical Geosciences, 46, 59–73.

Zuber, M. T., Smith, D. E., Solomon, S. C., Muhleman, D. O., Head, J. W., Garvin, J.B., et al. (1992). The Mars Observer Laser Altimeter investigation. Journal of Geophysical Research, 97, 7781–7797.

Table 1.

Compilation of structural parameters calculated for the studied Amenthes Region faults.

			Fault parameters				Trishear parameters				
Name	Length (km)	Max. relief (m)	Strike (º)	Dip angle (º)	Depth of faulting (km)	Max. Slip (m)	Trishear angle (º)	Trishear distribution		P/S ratio	Fault tip depth (m)
								θ_1	θ_2		
Main fault (Amenthes Rupes)	470	1050	N131 E	27–28 NE	20–24	2100	86	72	14	3	-2050
Fault 2 (splay)	180	570	N120 E	29.5 NE	23.5–24	1300	85	71.5	13.5	2	-1180
Fault 3 (backthrust)	220	900	N138 E	31–33 SW	21.5–22.5	1600	80	40	40	3	-2100
Fault 4	126	800	N125 E	23 NE	13	1720	44	28.5	15.5	2	-2700
Fault 5 Segment NW	180	600	N122 E	28 NE	10.5–11.5	1100	85	33	52	2	-940
Fault 5 Segment SE	160	480	N131 E	27–27.5 NE	9.5–11	1000	60	42	18	2	-1800

825

Table 2.

Fault parameters obtained in different studies performed on Amenthes Rupes.

	Maximum slip (m)	Dip angle (º)	Depth of faulting (km)
Amenthes Rupes (Schultz & Watters, 2001)	1500	25–30	25–30
Amenthes Rupes (Ruiz et al., 2008)	1900–2300	19–24	27–35
Amenthes Rupes (Mueller et al., 2014)	1170–1440	41.5–56.1	33–48
Amenthes Rupes (Egea González et al., 2017)	1500–2000	20–35	27–33
Amenthes Rupes (This study)	2100	27–28	20–24
Amenthes Region-Fault 2 (This study)	1300	29.5	23.5–24
Amenthes Region- Fault 3 (This study)	1600	31–33	21.5–22.5

826

Figure 1. Structural map of the study area of Amenthes Region. The base map is made by combining a MOLA model (DEM) over a THEMIS-IR Day image. The thrust faults included in the modeling are colored in red. The inset globe shows the location of the study area.

Figure 2. Schematic representation of trishear method (based on Hardy & Ford, 1997; Zehnder & Allmendinger, 2000). The area colored in grey is the trishear area and it is defined by the trishear angle (θ) and its distribution between the hanging wall and the footwall (θ_1, θ_2). The propagating fault tip is marked in blue. The velocity of the hanging wall relative to the footwall is marked by a grey slip vector, decreasing from top to bottom inside the trishear area.

Figure 3. a. Original MOLA surface over a THEMIS-IR Day image of the studied area. **b.** Restored topographic surface where the uplifts present in the original MOLA model, which are related to the studied thrust faults, have been removed.

Figure 4. a. Perspective of the 3D model of the studied area where MOLA topographic surface has been hidden southeastern from the profile A-A' to show the underlying fault planes of the main fault, Fault 2, Fault 3 and Fault 4. **b.** Cross section A-A' perpendicular to the mean strike of the faults. **c.** Perspective of the 3D model where the MOLA surface has been hidden southeastern from the profile B-B'. All the fault planes of the 3D modeling are visible. **d.** Rose diagram representing the dip azimuth of the 3D fault planes included in the modeling. The mean dip azimuth (N36.6ºE) is shown with a black arrow. **e.** Cross section B-B', perpendicular to the mean strike of the studied faults.

Figure 5. a. Colored topographic surface used as a base for the forward modeling procedure where the uplifts associated with the slip of the thrust faults have been removed together with the craters in the area. **b.** Topographic surface resulting from the 3D forward modeling, where the original MOLA surface is reproduced from the 5.a. surface.

Figure 6. Lengthwise profile of the Amenthes thrust fault system showing the slip distribution obtained for each of the five faults included in the modeling.

Figure 7. Absolute elevation difference between the original MOLA topographic surface and the model obtained from the 3D forward modeling. Perfect fit between the model and the observed topography is represented by zero values.

Figure 8. Representation of the total horizontal shortening estimate in a lengthwise profile orthogonal to the general shortening direction, which corresponds with the mean strike of the fault system (N126.6ºE).

Figure 1.

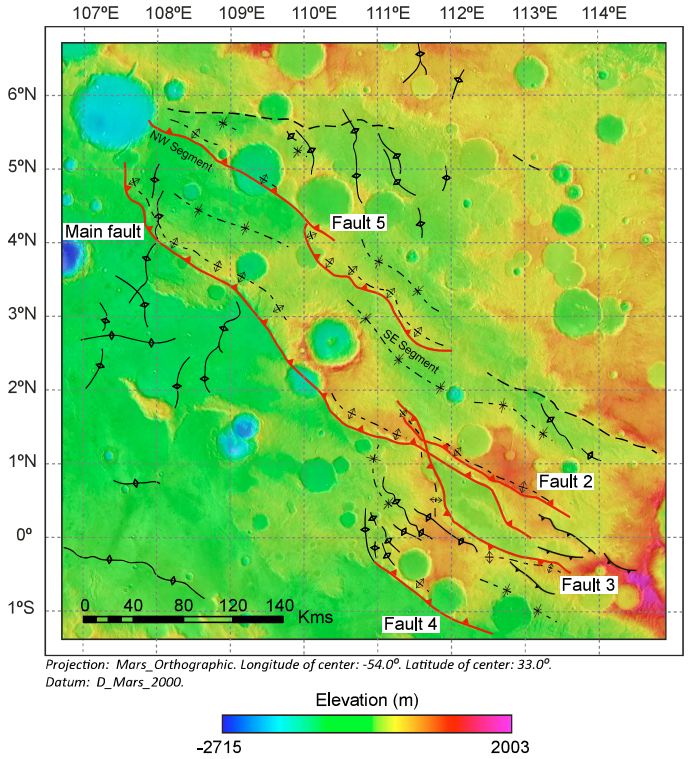

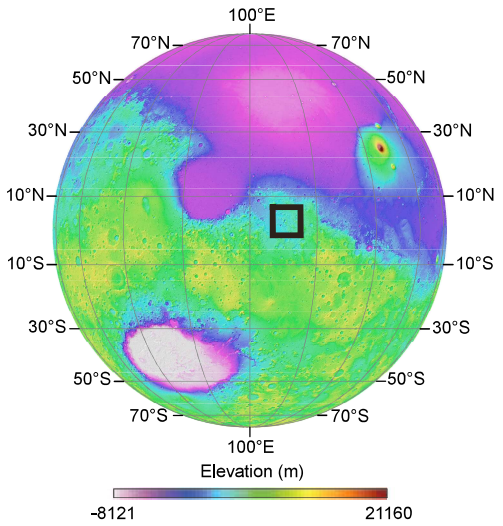

Tectonic structures

- Thrust fault
- Minor thrust fault
- Fault (approx.)
- Anticline
- Syncline
- Wrinkle ridges

Figure 2.

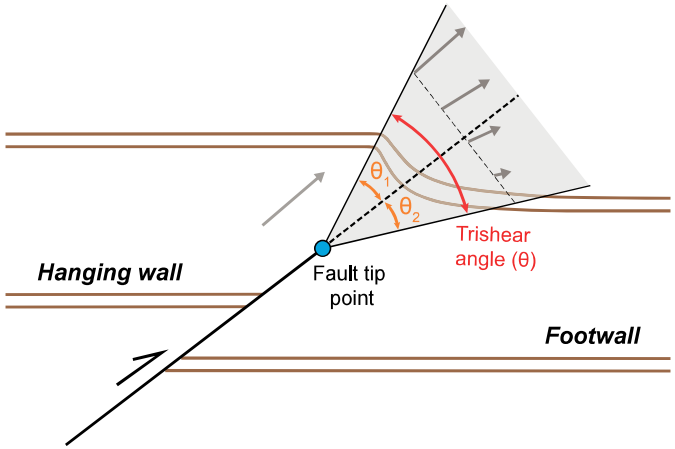
θ1
θ2
Trishear
angle (θ)
Hanging wall
Fault tip
point
Footwall

Figure 3.

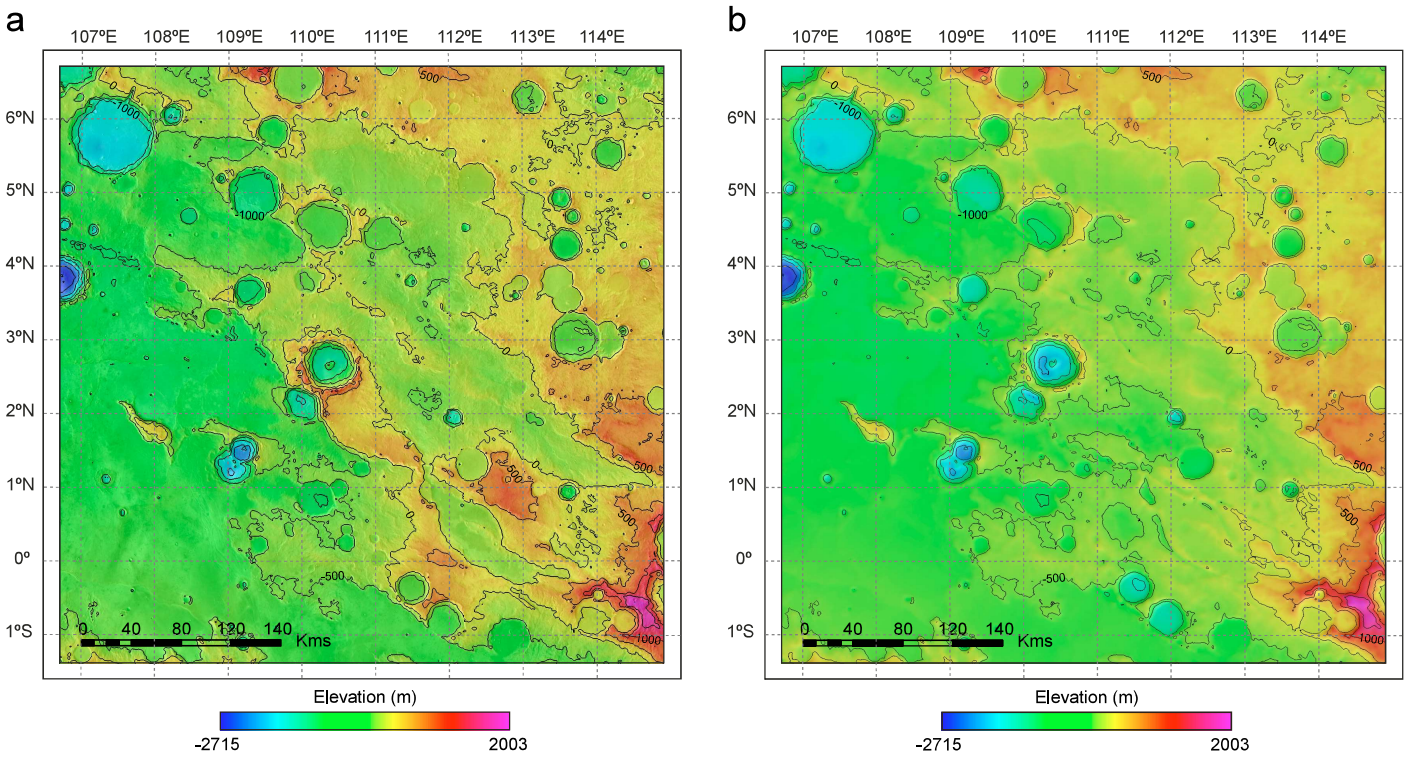
a
b
107ºE
108ºE
109ºE
110ºE
111ºE
112ºE
113ºE
114ºE
6ºN
5ºN
4ºN
3ºN
2ºN
1ºN
0º
1ºS
0
40
80
120
140
Kms
Elevation (m)
-2715
2003

Figure 4.

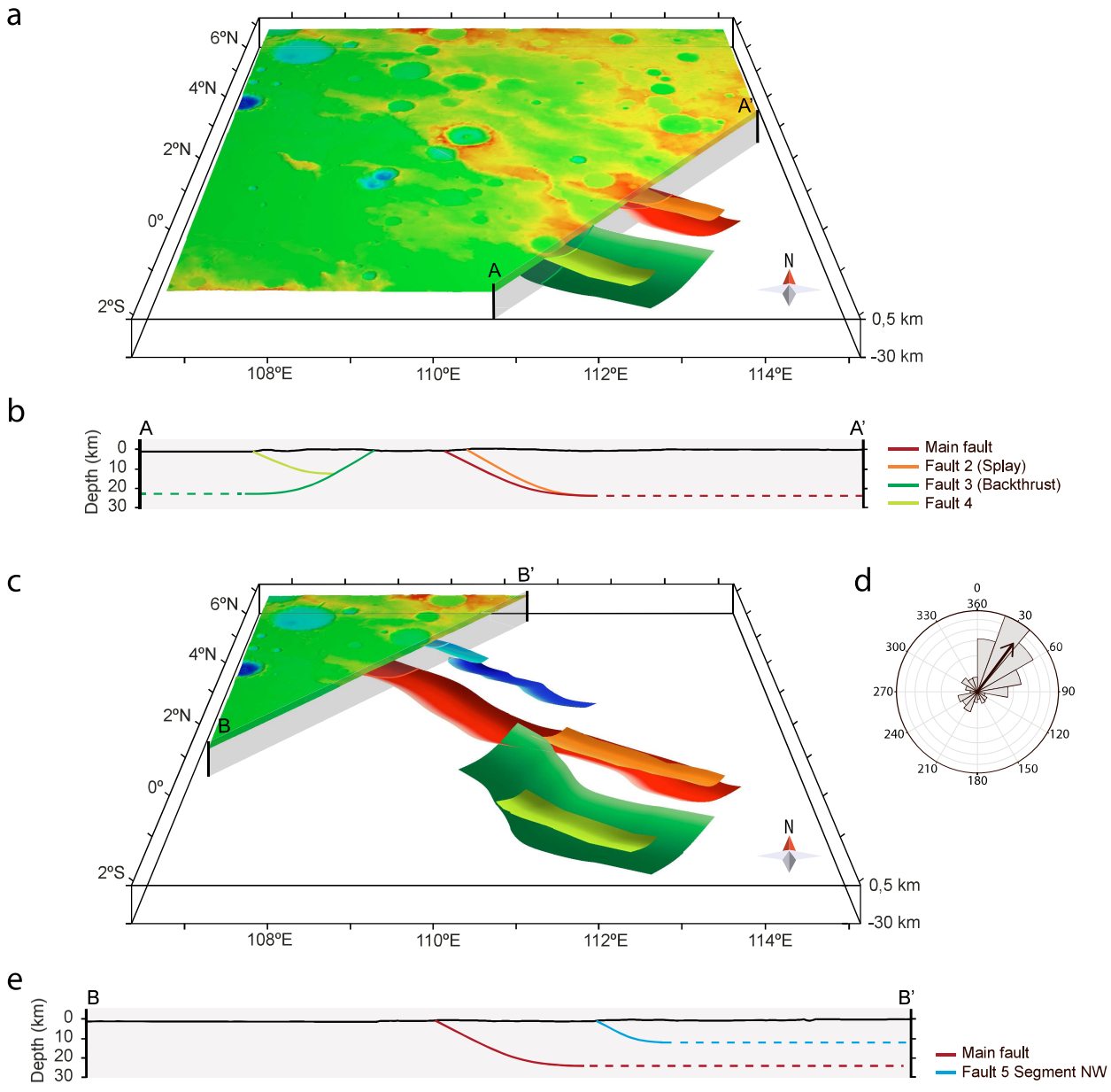
a
6ºN
4ºN
2ºN
0º
2ºS
A
A'
N
0,5 km
-30 km
108ºE
110ºE
112ºE
114ºE
b
A
A'
Depth (km)
0
10
20
30
Main fault
Fault 2 (Splay)
Fault 3 (Backthrust)
Fault 4
c
B'
B
d
0
30
60
90
120
150
180
210
240
270
300
330
360
e
B
B'
Fault 5 Segment NW

Figure 5.

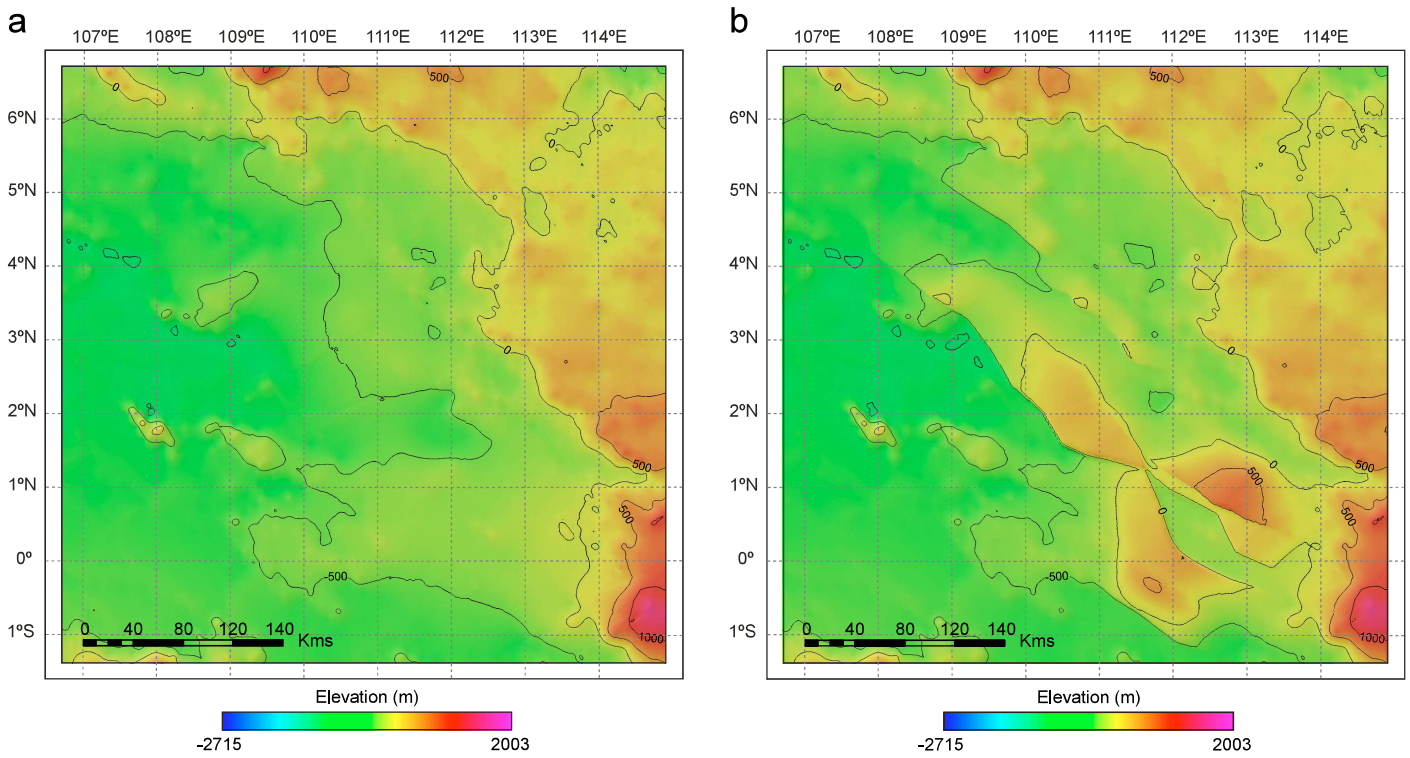
a
b
107ºE
108ºE
109ºE
110ºE
111ºE
112ºE
113ºE
114ºE
6ºN
5ºN
4ºN
3ºN
2ºN
1ºN
0º
1ºS
0
500
-500
1000
0 40 80 120 140
Kms
Elevation (m)
-2715
2003

Figure 6.

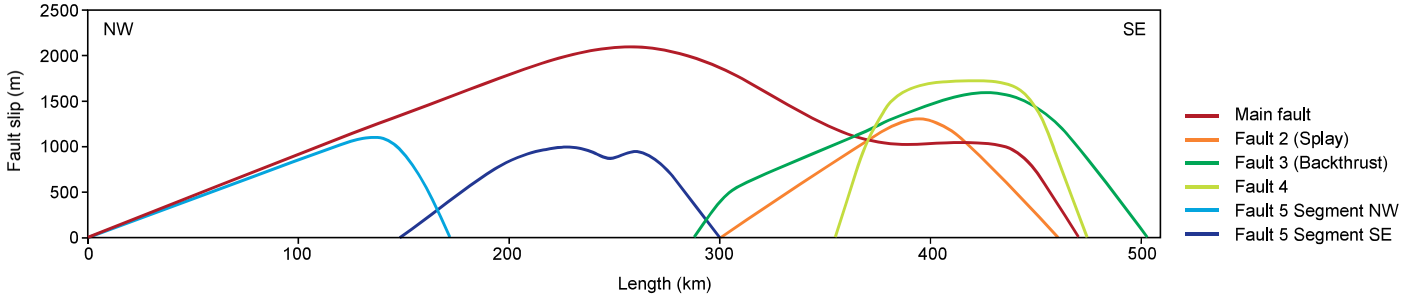
NW
SE
Fault slip (m)
2500
2000
1500
1000
500
0
0
100
200
300
400
500
Length (km)
Main fault
Fault 2 (Splay)
Fault 3 (Backthrust)
Fault 4
Fault 5 Segment NW
Fault 5 Segment SE

Figure 7.

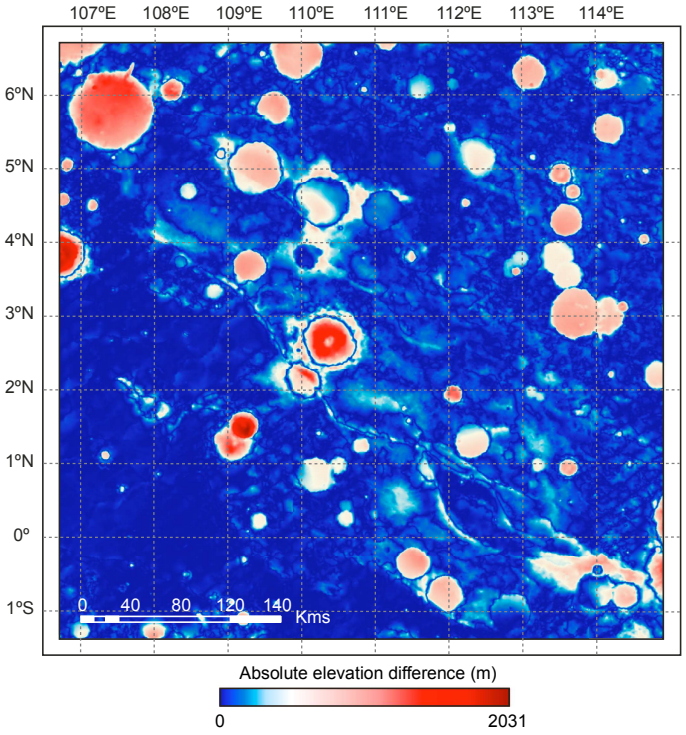
107ºE
108ºE
109ºE
110ºE
111ºE
112ºE
113ºE
114ºE
6ºN
5ºN
4ºN
3ºN
2ºN
1ºN
0º
1ºS
0
40
80
120
140
Kms
Absolute elevation difference (m)
0
2031

Figure 8.

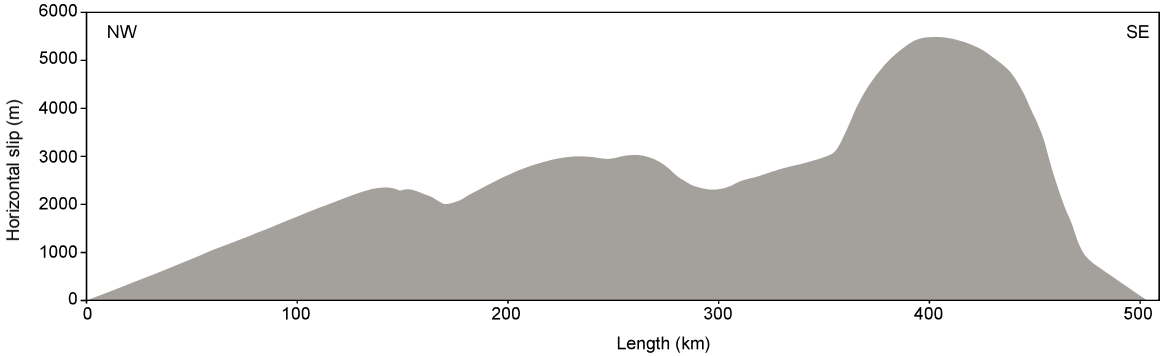
NW
SE
Horizontal slip (m)
6000
5000
4000
3000
2000
1000
0
0
100
200
300
400
500
Length (km)

Table 1.

Compilation of structural parameters calculated for the studied Amenthes Region faults.

			Fault parameters				Trishear parameters				
Name	Length (km)	Max. relief (m)	Strike (º)	Dip angle (º)	Depth of faulting (km)	Max. Slip (m)	Trishear angle (º)	Trishear distribution		P/S ratio	Fault tip depth (m)
								θ_1	θ_2		
Main fault (Amenthes Rupes)	470	1050	N131 E	27–28 NE	20–24	2100	86	72	14	3	-2050
Fault 2 (splay)	180	570	N120 E	29.5 NE	23.5–24	1300	85	71.5	13.5	2	-1180
Fault 3 (backthrust)	220	900	N138 E	31–33 SW	21.5–22.5	1600	80	40	40	3	-2100
Fault 4	126	800	N125 E	23 NE	13	1720	44	28.5	15.5	2	-2700
Fault 5 Segment NW	180	600	N122 E	28 NE	10.5–11.5	1100	85	33	52	2	-940
Fault 5 Segment SE	160	480	N131 E	27–27.5 NE	9.5–11	1000	60	42	18	2	-1800

Table 2.
Fault parameters obtained in different studies performed on Amenthes Rupes.

	Maximum slip (m)	Dip angle (º)	Depth of faulting (km)
Amenthes Rupes (Schultz & Watters, 2001)	1500	25–30	25–30
Amenthes Rupes (Ruiz et al., 2008)	1900–2300	19–24	27–35
Amenthes Rupes (Mueller et al., 2014)	1170–1440	41.5–56.1	33–48
Amenthes Rupes (Egea González et al., 2017)	1500–2000	20–35	27–33
Amenthes Rupes (This study)	2100	27–28	20–24
Amenthes Region-Fault 2 (This study)	1300	29.5	23.5–24
Amenthes Region- Fault 3 (This study)	1600	31–33	21.5–22.5